12 The Hartree-Fock approximation

12.1 Properties of single Slater determinants

Before deriving the Hartree-Fock equations is it useful to give some special cases of some diagonal matrix elements. The eigenstates of $H^{(0)}$ can be ordered with respect to the total energy $E^{(0)}$, with the lowest energy state being the one in which all of the particles occupy the lowest energy set of single-particle states allowed by the Pauli principle. This lowest-energy state will be denoted by $\mid C >$. (This notation derives from the fact that it will be associated with the closed-shell configuration.) The n single-particle states occupied in $\mid C >$ will be labeled by $\alpha, \beta, \gamma \ldots$. The total energy $E(C)$ of the state $\mid C >$ is

$$E(C) = < C \mid H \mid C > = \sum_{\alpha} < \alpha \mid T \mid \alpha > + \frac{1}{2} \sum_{\alpha\beta} < \alpha\beta \mid V \mid \alpha\beta > . \tag{12.1}$$

I will use i and j to label specific states above or below the fermi surface which will be considered explicitly in the summations. The total energy of a system with the configuration $\mid C >$ plus one particle in the state i above the fermi surface (a state unoccupied in $\mid C >$) is

$$\begin{aligned} E(Ci) &= < Ci \mid H \mid Ci > \\ &= E(C) + < i \mid T \mid i > + \sum_{\alpha} < i\alpha \mid V \mid i\alpha > . \end{aligned} \tag{12.2}$$

The difference between $E(Ci)$ and $E(C)$ will be denoted by, ϵ(i), the single-particle energy:

$$\epsilon(i) = E(Ci) - E(C) = < i \mid T \mid i > + \sum_{\alpha} < i\alpha \mid V \mid i\alpha > . \tag{12.3}$$

The total energy of a system with the configuration $\mid C >$ plus particles in the states i and j above the fermi surface is

$$\begin{aligned} E(Cij) &= < Cij \mid H \mid Cij > \\ &= E(C) + < i \mid T \mid i > + \sum_{\alpha} < i\alpha \mid V \mid i\alpha > \\ &+ < j \mid T \mid j > + \sum_{\alpha} < j\alpha \mid V \mid j\alpha > + < ij \mid V \mid ij > \\ &= E(C) + \epsilon(i) + \epsilon(j) + < ij \mid V \mid ij > \end{aligned} \tag{12.4}$$

The total energy of a system with the configuration $\mid C >$ with one particle absent in the state i (normally occupied in $\mid C >$) is

$$E(Ci^{-1}) = < Ci^{-1} \mid H \mid Ci^{-1} >$$

$$= E(C) - < i \mid T \mid i > - \sum_{\alpha} < i\alpha \mid V \mid i\alpha > . \tag{12.5}$$

The difference between $E(Ci^{-1})$ and $E(C)$ will be denoted by, ϵ(i):

$$\epsilon(i) = E(C) - E(Ci^{-1}) =< i \mid T \mid i > + \sum_{\alpha} < i\alpha \mid V \mid i\alpha >, \tag{12.6}$$

which has the same form as the single-particle energy. Finally, the total energy of a system with the configuration $\mid C >$ plus particles absent in the states i and j is

$$\begin{aligned} E(Ci^{-1}j^{-1}) &=< Ci^{-1}j^{-1} \mid H \mid Ci^{-1}j^{-1} > \\ &= E(C) - \epsilon(i) - \epsilon(j) + < ij \mid V \mid ij > \end{aligned} \tag{12.7}$$

12.2 Derivation of the Hartree-Fock equations

In the Hartree-Fock approximation, $E(C)$ is minimized with respect to variation of the single-particle wave functions $\phi_i(\vec{r})$ [or equivalently with respect to $\phi_i{}^*(\vec{r})$]. With the coordinate space matrix elements of T and V, one obtains

$$\frac{\partial}{\partial \phi_i^*(\vec{r})} \left\{ E(C) - \sum_{\alpha} \lambda_\alpha \int \mid \phi_\alpha(\vec{r}_1) \mid^2 \, d\tau_1 \right\} = 0$$

$$\begin{aligned} &= T\phi_i(\vec{r}) - \lambda_i \phi_i(\vec{r}) + \frac{1}{2} \Big\{ \sum_{\beta} \int \phi_\beta^*(\vec{r}_2)\, V(\vec{r}\vec{r}_2)\, \phi_i(\vec{r})\, \phi_\beta(\vec{r}_2)\, d\tau_2 \\ &+ \sum_{\alpha} \int \phi_\alpha^*(\vec{r}_1)\, V(\vec{r}_1\vec{r})\, \phi_\alpha(\vec{r}_1)\phi_i(\vec{r})\, d\tau_1 - \sum_{\beta} \int \phi_\beta^*(\vec{r}_2)\, V(\vec{r}\vec{r}_2)\, \phi_\beta(\vec{r})\, \phi_i(\vec{r}_2)\, d\tau_2 \\ &- \sum_{\alpha} \int \phi_\alpha^*(\vec{r}_1)\, V(\vec{r}_1\vec{r})\, \phi_i(\vec{r}_1)\, \phi_\alpha(\vec{r})\, d\tau_1 \Big\}, \end{aligned} \tag{12.8}$$

where λ are Lagrange multipliers which are introduced to enforce the normalization. Using $V(\vec{r}_1\ \vec{r}_2) = V(\vec{r}_2\ \vec{r}_1)$, this reduces to

$$\begin{aligned} &T\phi_i(\vec{r}) + \left\{ \sum_{\alpha} \int \phi_\alpha^*(\vec{r}_1) V(\vec{r}\vec{r}_1) \phi_\alpha(\vec{r}_1)\, d\tau_1 \right\} \phi_i(\vec{r}) \\ &- \int \left\{ \sum_{\alpha} \phi_\alpha^*(\vec{r}_1) V(\vec{r}\vec{r}_1) \phi_\alpha(\vec{r}) \right\} \phi_i(\vec{r}_1)\, d\tau_1 = \lambda_i \phi_i(\vec{r}). \end{aligned} \tag{12.9}$$

This nonlocal differential equation can be used to solve for λ_i and $\phi_i(\vec{r})$. It can be solved in an iterative fashion: (i) choose some initial guess for $\phi_i(\vec{r})$ and calculate the integrals as a function of $\vec{r}$, (ii) solve the differential equation for λ_i and $\phi_i(\vec{r})$, (iii) recalculate the integrals, and (iv) iterate until the λ_i and $\phi_i(\vec{r})$ converge.

Multiplying Eq. (12.9) by $\phi_i^*(\vec{r})$ on both sides and integrating gives

$$< i \mid T \mid i > + \sum_\alpha < i\alpha \mid V \mid i\alpha > = \lambda_i = \epsilon(i), \tag{12.10}$$

where the Lagrange multiplier has been equated to the single-particle energy by comparison to Eqs. (12.3) and (12.6). The term $\sum_\alpha < i\alpha \mid V \mid i\alpha >$ can be identified as the expectation value of the mean-field potential U'.

$$< i \mid U' \mid i > = < i \mid U^{\rm HF} \mid i > = \sum_\alpha < i\alpha \mid V \mid i\alpha > . \tag{12.11}$$

Thus, the full Hartree-Fock hamiltonian is

$$H = H^{(0)} + W, \tag{12.12}$$

with

$$H^{(0)} = \sum_k (T + U^{\rm HF})_k, \tag{12.13}$$

and

$$W = \sum_{kl} V_{kl} - \sum_k U_k^{\rm HF}. \tag{12.14}$$

The state $\mid C >$ with the Hartree-Fock condition of Eq. (12.11) enforced will be denoted by $\mid \Phi_{\rm HF} >$. The zeroth-order and first-order matrix elements are

$$E_{\rm HF}^{(0)} = < \Phi_{\rm HF} \mid \sum_k (T + U^{\rm HF})_k \mid \Phi_{\rm HF} > = \sum_\alpha \epsilon(\alpha), \tag{12.15}$$

and

$$\begin{aligned} E_{\rm HF}^{(1)} &= < \Phi_{\rm HF} \mid W \mid \Phi_{\rm HF} > = < \Phi_{\rm HF} \mid \sum_{kl} V_{kl} - \sum_k (U^{\rm HF})_k \mid \Phi_{\rm HF} > \\ &= \frac{1}{2} \sum_{\alpha\beta} < \alpha\beta \mid V \mid \alpha\beta > - \sum_\alpha < \alpha \mid U^{\rm HF} \mid \alpha > \\ &= -\frac{1}{2} \sum_{\alpha\beta} < \alpha\beta \mid V \mid \alpha\beta > . \end{aligned} \tag{12.16}$$

The total unperturbed energy can thus be expressed in several ways:

$$\begin{aligned} E_{\rm HF}^{(0)} + E_{\rm HF}^{(1)} &= \sum_\alpha \epsilon(\alpha) - \frac{1}{2} \sum_{\alpha\beta} < \alpha\beta \mid V \mid \alpha\beta > \\ &= \sum_\alpha < \alpha \mid T \mid \alpha > + \frac{1}{2} \sum_{\alpha\beta} < \alpha\beta \mid V \mid \alpha\beta > \end{aligned}$$

$$= \frac{1}{2}\left\{\sum_{\alpha}\epsilon(\alpha) + \sum_{\alpha} < \alpha \mid T \mid \alpha >\right\}. \tag{12.17}$$

It is to be noted that the Hartree-Fock condition does not make $E^{(1)}$ vanish. The advantage of the Hartree-Fock procedure is that an important class of matrix elements $< \Phi_{\rm HF} \mid W \mid \Phi >$ which enter into the second-order corrections vanish − namely, all of those for which Φ differs from $\Phi_{\rm HF}$ by the addition of one particle above the fermi surface and the removal of one particle below the fermi surface. These are called one-particle one-hole, 1p-1h, configurations. The most important corrections are those in which the Φ differs from $\Phi_{\rm HF}$ by addition of two-particle above the fermi surface and the removal of two particles below the fermi surface (2p-2h configurations).

12.3 Examples of single-particle energies

The Hartree-Fock model works best for those nuclei where there is a large gap at the fermi surface for both protons and neutrons. The total energies for the closed shell, one-particle and one-hole configurations are the interaction energies E measured for the respective, nuclei, where $BE = -E$. For example, if we take ^{16}O as a doubly closed shell nucleus, then energies obtained from the ground state binding energies are:

$$E(^{16}O) = E(C) = -127.619 \text{ MeV}$$

$$E(^{17}O) = E[C, 0d_{5/2} \text{ neutron}] = -131.763 \text{ MeV}$$

$$E(^{17}F) = E[C, 0d_{5/2} \text{ proton}] = -128.220 \text{ MeV}$$

$$E(^{15}O) = E[C, (0p_{1/2})^{-1} \text{ neutron}] = -111.956 \text{ MeV}$$

$$E(^{15}N) = E[C, (0p_{1/2})^{-1} \text{ proton}] = -115.492 \text{ MeV}$$

where the n, ℓ, j values are inferred from the spin-parity of the odd-even ground states. The experimental single-particle energies for these states are thus:

$$\epsilon(0d_{5/2} \text{ neutron}) = E(^{17}O) - E(^{16}O) = -4.144 \text{ MeV}$$

$$\epsilon(0d_{5/2} \text{ proton}) = E(^{17}F) - E(^{16}O) = -0.601 \text{ MeV}$$

$$\epsilon(0p_{1/2} \text{ neutron}) = E(^{16}O) - E(^{15}O) = -15.663 \text{ MeV}$$

$$\epsilon(0p_{1/2} \text{ proton}) = E(^{16}O) - E(^{15}N) = -12.127 \text{ MeV}$$

The single-particle energies for other states can be inferred form the energies E associated with excited states in the A=15 and A=17 nuclei.

It will be shown in a homework that Eq. (12.17) is in fact not satisfied by experimental data in nuclear physics, when the ϵ are taken from experiment and when

the kinetic energies are calculated. This means that higher-order corrections to the Hartree-Fock are important. If these corrections are taken into account by using an effective hamiltonian, this hamiltonian will need to include three-body and/or density dependent terms. An example is the Skyrme interaction which includes a density-dependent interaction.

12.4 Results with the Skyrme hamiltonian

The Skyrme approximation [1], [2] is an $s-$ and $p-$wave expansion of an effective two-body interaction together with an $s-$wave density dependent interaction:

$$V_{\rm Skyrme} = t_0(1+x_0P_\sigma)\delta + \frac{1}{2}t_1(1+x_1P_\sigma)\left(\mathbf{k}'^2\,\delta + \delta\,\mathbf{k}^2\right)$$
$$+t_2(1+x_2P_\sigma)\,\mathbf{k}'\cdot\delta\,\mathbf{k} + \frac{1}{6}t_3(1+x_3P_\sigma)\,\rho^\alpha(\mathbf{R})\,\delta$$
$$+iW_0(\sigma_i+\sigma_j)\cdot\mathbf{k}\times\delta\mathbf{k} + V^{Coul}, \tag{12.18}$$

where $\delta = \delta(\mathbf{r}_i - \mathbf{r}_j)$, $\mathbf{k} = (1/2i)(\nabla_i - \nabla_j)$ is the relative momentum operator acting on the wave function to the right and $\mathbf{k}'$ is the adjoint of $\mathbf{k}$. P_σ is the spin-exchange operator and $\mathbf{R} = (\mathbf{r}_i + \mathbf{r}_j)/2$. The form of the Skyrme interaction allows one to calculate the potentials analytically in terms of the densities which makes the self-consistent calculations fast.

The Skyrme interaction results in a non-local potential for protons ($q = p$) and neutrons ($q = n$) given by $U_q(r) + U'_q(r)$ with

$$U_q(r) = t_0\left(\left[1+\frac{x_0}{2}\right]\rho - \left[x_0+\frac{1}{2}\right]\rho_q\right)$$
$$+\frac{t_1}{8}\left(\left[1+\frac{x_1}{2}\right][2\tau - 3(\Delta\rho)] - \left[x_1+\frac{1}{2}\right][2\tau_q - 3(\Delta\rho_q)]\right)$$
$$+\frac{t_2}{2}\left(\left[1+\frac{x_2}{2}\right][2\tau + (\Delta\rho)] + \left[x_2+\frac{1}{2}\right][2\tau_q + (\Delta\rho_q)]\right)$$
$$+\frac{t_3}{6}\left(\left[1+\frac{x_3}{2}\right]\rho - \left[x_3+\frac{1}{2}\right]\rho_q\right)\rho^\alpha - \frac{W_0}{2}\nabla\cdot(\mathbf{J}+\mathbf{J}_q)$$
$$+U_q^{Coul}(r) + U_q^{so}(r)[\ell\cdot\sigma] \tag{12.19}$$

and

$$U'_q(r) = -\nabla\cdot\left\{\frac{t_1}{4}\left(\left[1+\frac{x_1}{2}\right]\rho - \left[x_1+\frac{1}{2}\right]\rho_q\right)\right.$$
$$\left.+\frac{t_2}{4}\left(\left[1+\frac{x_2}{2}\right]\rho + \left[x_2+\frac{1}{2}\right]\rho_q\right)\right\}\nabla, \tag{12.20}$$

where the spin-orbit potential is:

$$U_q^{so}(r) = \frac{1}{r}\left\{\frac{W_0}{2}\left[\frac{d}{dr}(\rho+\rho_q)\right] + \frac{1}{8}\left[(t_1-t_2)J_q\right] - \frac{1}{8}\left[t_1x_1 + t_2x_2\right]J\right\} \tag{12.21}$$

The U' term of Eq. (12.20) can be combined with the kinetic energy operator to write Eq. (12.9) in terms of the a Schroedinger-like equation with an effective mass:

$$\left\{-\nabla \cdot \frac{\hbar^2}{2m_q^*(r)}\nabla + U_q(r)\right\}\phi_{i,q}(\mathbf{r}) = \epsilon_{i,q}\ \phi_{i,q}(\mathbf{r}). \tag{12.22}$$

where the effective mass is defined by:

$$\frac{\hbar^2}{2m_q^*(r)} = \frac{\hbar^2}{2m} + \frac{t_1}{4}\left(\left[1+\frac{x_1}{2}\right]\rho - \left[x_1+\frac{1}{2}\right]\rho_q\right)$$

$$+\frac{t_2}{4}\left(\left[1+\frac{x_2}{2}\right]\rho + \left[x_2+\frac{1}{2}\right]\rho_q\right) \tag{12.23}$$

The densities in these equations are

$$\rho_q(r) = \sum_\alpha \mid \phi_{q\alpha}(r) \mid^2, \tag{12.24}$$

$$\tau_q(r) = \sum_\alpha \mid \nabla\phi_{q\alpha}(r) \mid^2 \tag{12.25}$$

$$\mathbf{J}_q(r) = i\sum_\alpha \phi^*_{q\alpha}(r)[\sigma \times \phi_{q\alpha}(\mathbf{r})], \tag{12.26}$$

$$\rho(r) = \rho_p(r) + \rho_n(r), \tag{12.27}$$

$$\tau(r) = \tau_p(r) + \tau_n(r), \tag{12.28}$$

$$\mathbf{J}(r) = \mathbf{J}_p(r) + \mathbf{J}_n(r), \tag{12.29}$$

and

$$(\Delta f) = \frac{1}{r}\left[\frac{d^2}{dr^2} r f(r)\right], \tag{12.30}$$

where the derivative operates only inside the brackets.

Eq. (12.22) can be rewrittin in terms of the Schroedinger equation with an energy-dependent potential [3]:

$$\left\{-\frac{\hbar^2}{2m_q}\nabla^2 + U_q^*(r,\epsilon)\right\}\phi_{i,q}(\mathbf{r}) = \epsilon_{i,q}\ \phi_{i,q}(\mathbf{r}), \tag{12.31}$$

where

$$U_q^*(r,\epsilon) = \frac{m_q^*(r)}{m}\Big[U_q(r) + \frac{1}{2}\left(\frac{d^2}{dr^2}\frac{\hbar^2}{2m_q^*(r)}\right)$$

$$-\frac{m_q^*(r)}{2\hbar^2}\left(\frac{d}{dr}\frac{\hbar^2}{2m_q^*(r)}\right)^2\Big] + \left[1-\frac{m_q^*(r)}{m}\right]\epsilon_{i,q} \tag{12.32}$$

Table 1: Values of the Skyrme parameters obtained with SKX .

Parameter	SKX	SKX error
α	0.5	
t_0	−1444.0	1.0
t_1	251.3	1.9
t_2	−131.4	1.2
t_3	12043.9	18.1
W_o	149.4	2.7
x_0	0.364	0.021
x_1	0.521	0.171
x_2	0.131	0.013
x_3	0.088	0.051

The goal of the Skyrme HF formulation is to write the HF equations in terms of a few parameters (the ten in Eq. (12.18)) that can be obtained from a least-squares fit to some selected set of experimental data. In principle one would like to derive the Skyrme parameters from the experimental nucleon-nucleon interaction. This involves understanding the effect of the trucation of the actual many-body wave function to the closed-shell structure assumed in the derivation. It also requires an understanding of the contributions of real three-body forces. There has not yet been a quantitative derivation of the Skyrme parameters from the first principles. The Skyrme formulation is a specific type of density-functional model which have been widely used in atomic, molecular and condensed matter physics. One can show that such functionals exist even if they cannot be explicitly derived [4], [5].

The have been many attemps to obtain the Skyrme parameters from various types of experimental data. In this book I will concentrate on two recent results. One is the SKX hamiltonian which is obtained by applying the above equations to the eleven closed-shell nuclei: ^{16}O, ^{34}Si, ^{40}Ca, ^{48}Ca, ^{48}Ni, ^{88}Sr, ^{100}Sn, ^{132}Sn and ^{208}Pb. The data include the binding energies of these nuclei, together with five rms charge radii and 65 single-particle energies. Ten parameters in Eq. (12.18) were varied (although only six linear-combinations are well determined). The SKX spin-orbit energy-density leaves out terms involving t_1, t_2, x_1 and x_2, and a generalized two-parameter spin-orbit force based upon the Hartree reduction was used [6]. SKX uses the Friedman-Pandharipande neutron matter equation of state [7] as a constraint (it has recently been shown that the neutron skin is sensitive to the properties of the neutron equation of state [8], [9]). SKX also introduces a new parameter which is needed to reproduce the mirror displacement energies by the addition of a charge symmetry breaking (CSB) interaction (SkXcsb [10]). The values of the Skyrme parameters for SKX are given in Table 1.

Goriely et al. [11] obtained the parameter set called MSk7. In addition to the formulation given above for closed-shell nuclei, the effect of nuclear pairing and deformation were also taken into account. The MSk7 parameters are based on a fit to the binding energies of 1772 nuclei (the radii or single-particle energies were not included). Of the ten parameters in Eq. (12.18), seven were varied (x_0 and x_1 were fixed at -0.5 and α was fixed at $1/3$). The spin-orbit energy density retains the terms involving t_1, t_2, x_1 and x_2, a four-parameters δ-function pairing force was added, and a two-parameter Wigner correction term was added. The MSk7 interaction was used to calculate the binding energies and shapes of 9200 nuclei [11]. The results were shown as the HF1 calculation in Chapter 1.

The relativistic mean-field is an alternative to the Skyrme HF. The relativistic description of nuclear systems uses a field theoretical approach (quantum hydrodynamics) where the interaction of nucleons is described by an exchange of mesons. [12] I will use the non-linear parameter set NL3 [13] which gives a good description of binding energies and radii.

12.4.1 Binding energies

The binding energies for the region of nuclei up to $A = 60$ vary by hundreds of MeV, yet we consider theoretical calculations which reproduce experiment to the level of several hundred keV to an MeV. The "coast to coast" situation for all nuclei between the drip lines is illustrated in Fig. (12.1) where the BE obtained with the MSk7 HF calculations [11] are shown for all nuclei between the proton and neutron drip lines centered on $Z = 20$ (left-hand side) and $N = 20$ (right-hand side) and compared to experiment where known.

The drip line is reached in each case when the derivative of the BE curve with respect to proton or neutron number goes to zero. One observes in the bottom panels of Fig. (12.1) an apparently featureless and smooth curve with the data in agreement with theory. However, we are interested in a much higher level of detail which is illustrated in the top panel by subtracting a smooth curve given by the liquid drop model (LDM) from theory and experiment. This top curve brings out the detail related the microscopic aspects of the nuclear shell model.

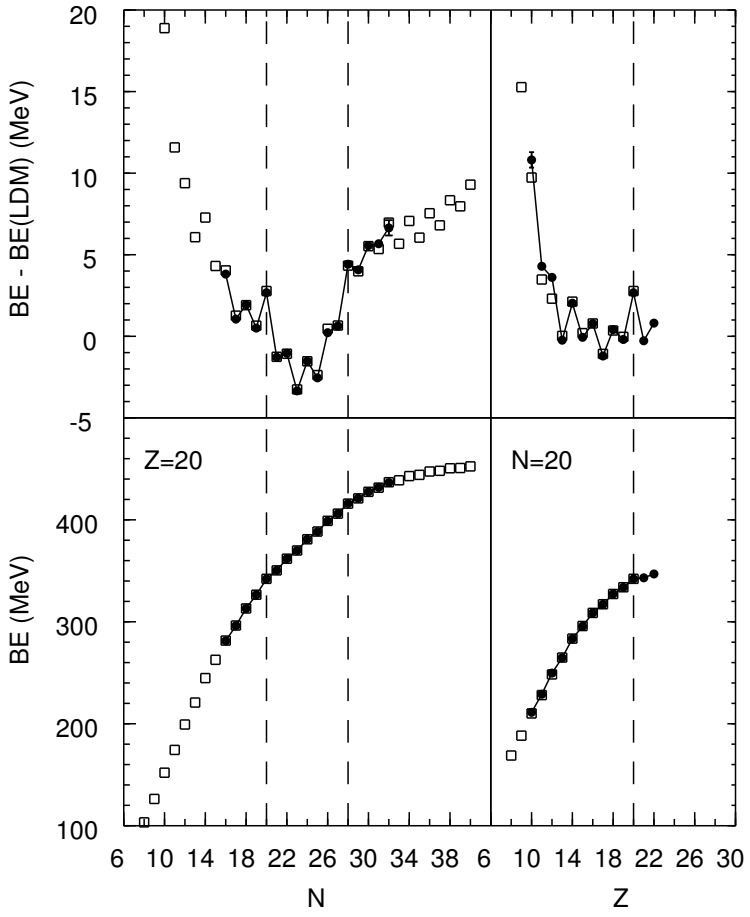

Figure 1: Theoretical (squares) and experimental (filled circles) binding energy for $Z = 20$ as a function of neutron number (left-hand side) and for $N = 20$ as a function of proton number (right-hand side). In the upper panels a smooth curve given by the liquid drop model is subtracted from theory and experiment. The magic numbers $N = 20$, $N = 28$ and $Z = 20$ are indicated by dashed lines.

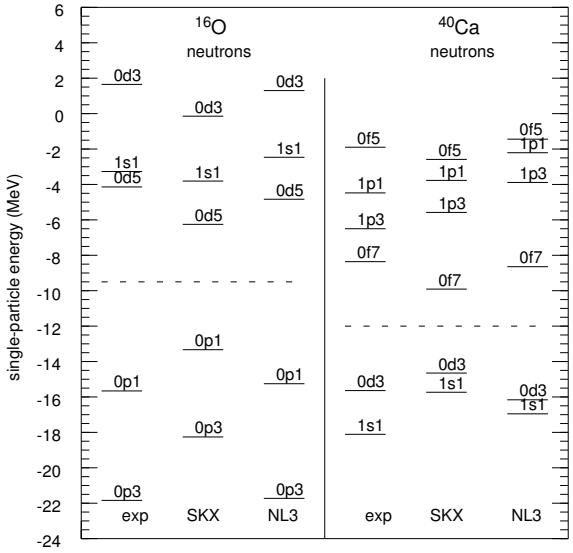

Figure 2: Experimental and theoretical neutron single-particle energies for ^{16}O and ^{40}Ca. The orbits are labeled by $(n, \ell, 2j)$, and the dashed line is the Fermi energy.

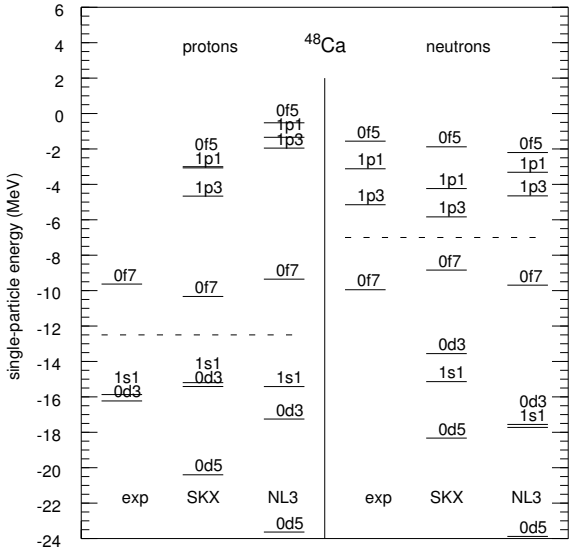

Figure 3: Experimental and theoretical proton and neutron single-particle energies for ^{48}Ca. The orbits are labeled by $(n, \ell, 2j)$, and the dashed line is the Fermi energy.

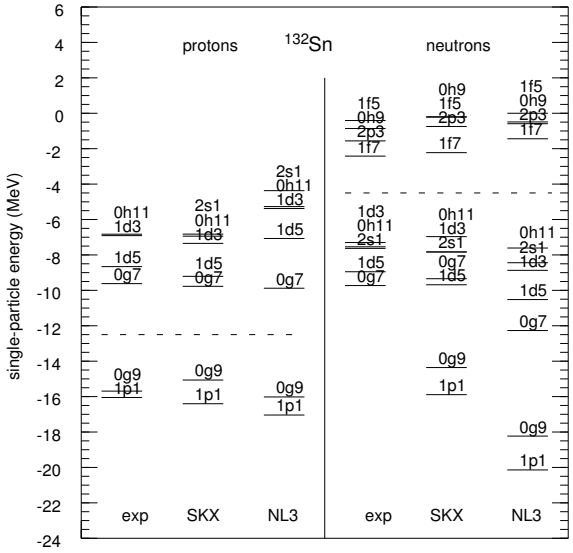

Figure 4: Experimental and theoretical proton and neutron single-particle energies for ^{132}Sn. The orbits are labeled by $(n, \ell, 2j)$, and the dashed line is the Fermi energy.

12.4.2 Single-particle energies

The experimental single-particle energies for ^{16}O, ^{40}Ca, ^{48}Ca, ^{132}Sn and ^{208}Pb are compared with the SKX Hartree-Fock and NL3 Dirac Hartree calculations in Figs. (12.2), (12.3), (12.4), and (12.5). Both mean-field calculations are in qualitative agreement with experiment. For light nuclei the NL3 results are in better, but for heavy nuclei the SKX results are better. The difference between SKX and NL3 is mainly related to the effective mass (m^*/m), which is about 1.0 for SKX and 0.6 for NL3. The effective mass for the Skyrme interaction can be tuned by the parameters [2] and those for SKX are determined primarily from the SPE of heavy nuclei where the spacing around the Fermi surface requires an effective mass of about 1.0 [14]. For NL3 on the other hand, an effective mass of about 0.6 is intrinsic to the model. An effective mass of 0.6 gives SPE in heavy nuclei which are spread out compared to experiment as shown by NL3 in Figs. (12.4) and (12.5). Typical Brueckner G matrix interactions also give an effective mass of about 0.6, and the reason for an empirical value of near unity in heavy nuclei is attributed to configuration mixing due to coupling of the single-particle states to surface vibrations [15], [16]. For a hamiltonian like SKX with an effective mass of unity, these surface vibrations effectively included in terms of a modified (renormalized) hamiltonian.

Experimental values of the SPE are usually used as input to shell-model calcula-

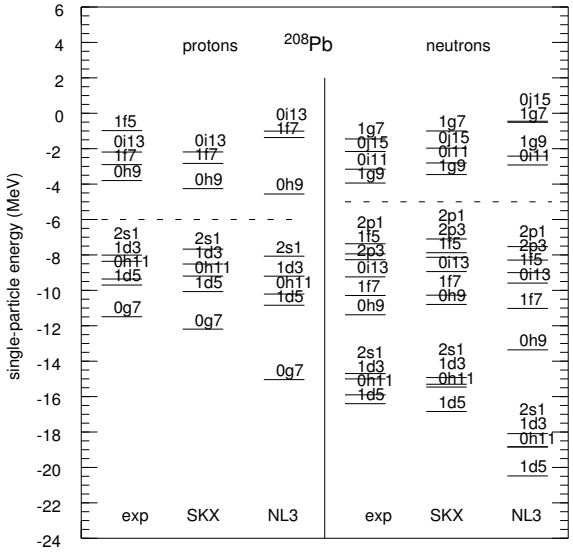

Figure 5: Experimental and theoretical proton and neutron single-particle energies for ^{132}Sn. The orbits are labeled by $(n, \ell, 2j)$, and the dashed line is the Fermi energy.

tions. For nuclei near the drip lines where the experimental SPE are not known, one needs a theoretical model for predicting or extrapolating the SPE. The HF parameter model such as SKX and NL3 provide perhaps the most reliable way to extrapolate the SPE from nuclei near stability to the most exotic nuclei near the drip lines. The predictions for the ^{60}Ca and ^{78}Ni SPE are given in Figs. (12.6) and (12.7), respectively. Other recent predictions for ^{60}Ca are given in [17]. It will remain for future experiments to test these extrapolations.

As a guide to the ordering of the single-particle states as a function of N and Z, I show in Fig. (12.8) the single-particle energies for nuclei with $N = Z$ obtained from with SKX . Fig. (12.9) shows the SKX single-particle energies for the calcium isotopes as a function of neutron number. Beyond ^{60}Ca one observes that the $0g_{9/2}$ orbital becomes bound, and thus ^{70}Ca will be bound with SKX . The even-even calcium nuclei between ^{60}Ca and ^{70}Ca will probably be bound due to pairing (which has been neglected in this particular SKX HF calculation).

12.4.3 Rms charge radii and charge densities

In this section I will discuss the results for rms charge and charge densities obtained with the Skyrme parameter sets SKX [14] and SKM* [18]

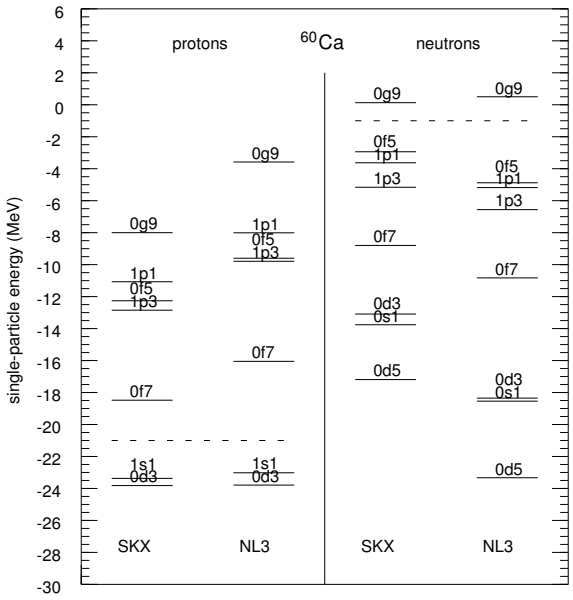

Figure 6: Theoretical proton and neutron single-particle energies for ^{60}Ca. The orbits are labeled by $(n, \ell, 2j)$, and the dashed line is the Fermi energy.

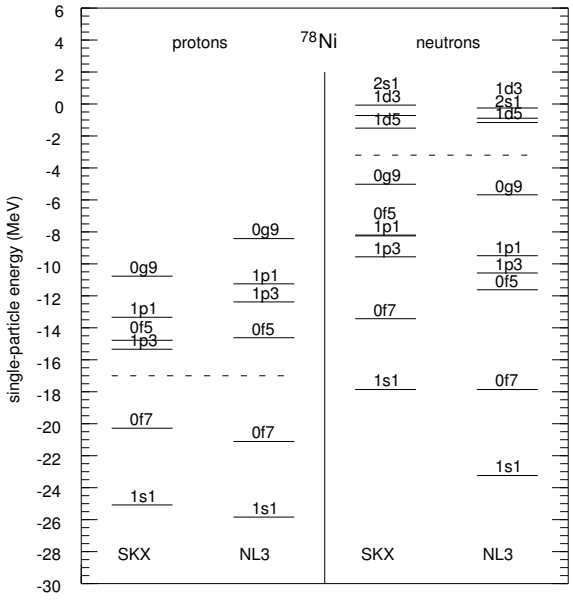

Figure 7: Theoretical proton and neutron single-particle energies for ^{78}Ni. The orbits are labeled by $(n, \ell, 2j)$, and the dashed line is the Fermi energy.

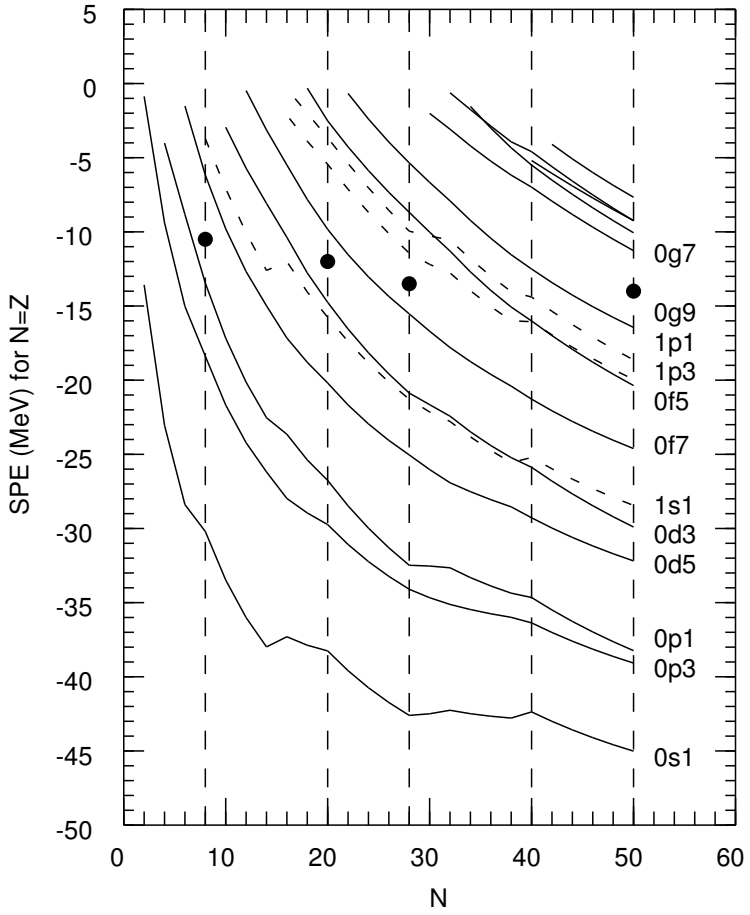

Figure 8: Neutron single-particle energies for nuclei with $N = Z$ as a function of neutron number obtained with the SKX spherical Hartree-Fock calculation. The vertical dashed lines show some of the magic number discussed in the text. The large circles show the approximate Fermi energies for ^{16}O, ^{40}Ca, ^{56}Ni and ^{100}Sn. The orbits are labeled by $(n, \ell, 2j)$.

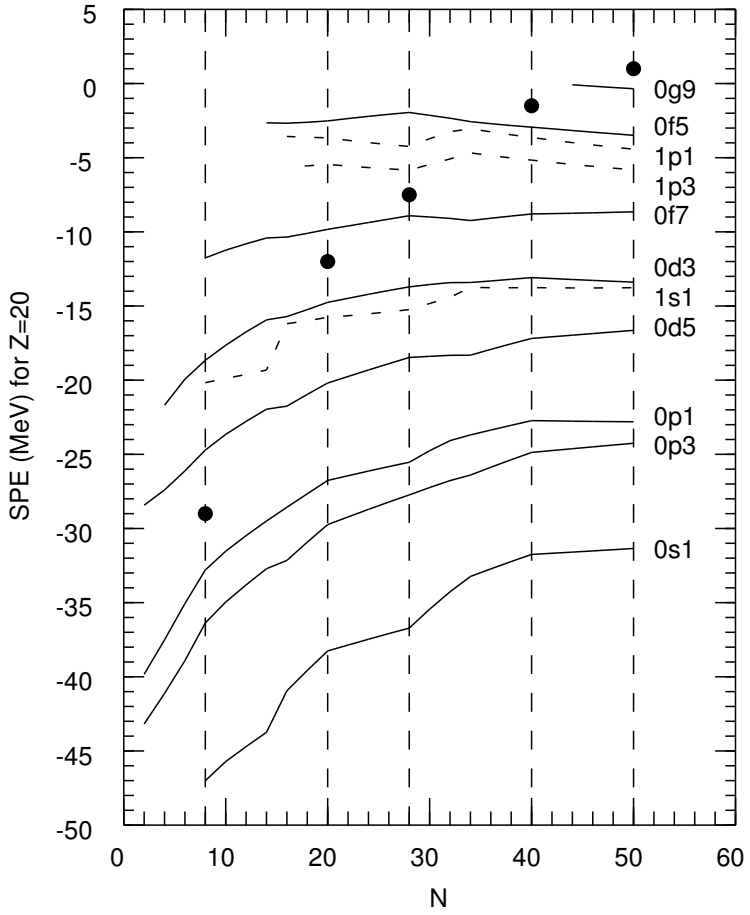

Figure 9: Neutron single-particle energies for the calcium isotopes obtained with the SKX spherical Hartree-Fock calculation. The vertical dashed lines show some of the magic number discussed in the text. The large circles show the approximate Fermi energies for ^{28}Ca, ^{40}Ca, ^{48}Ca, ^{60}Ca and ^{70}Ca. The orbits are labeled by $(n, \ell, 2j)$.

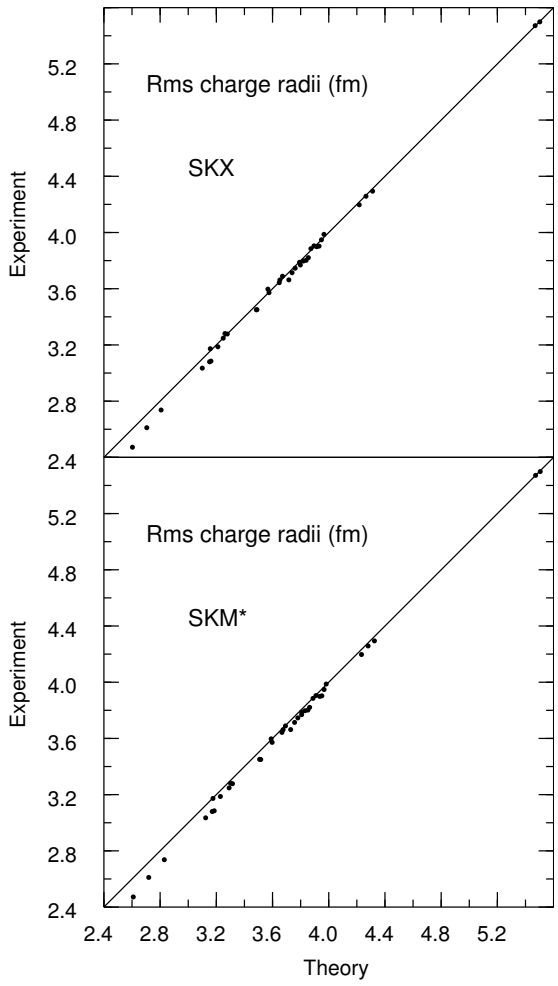

Figure 10: Comparison of experimental and theoretical rms charge radii for the Skyrme interactions SKX (top panel) and SKM* (bottom panel).

The experimental and theoretical rms charge radii are compared in Fig. (12.10). The experimental radii are from Refs. [19] and [20], with those with the smallest errors selected in the case of more than one data set. The error in the experimental data is typically smaller than the size of the data points. The Hartree-Fock results for the two interactions SKM* (bottom panel) and SKX (top panel) are obtained with the CM (fractional) occupations (those obtained with ESP occupations are essentially the same). The excellent overall agreement between experiment and theory is not surprising since these rms charge radii are used to constrain the values of the Skyrme parameters. The deviations increase for light nuclei going up to 5% for ^{12}C. In general one may expect the mean-field approximation to be less valid for light nuclei.

In order to illustrate how the features of the charge density are built out of the

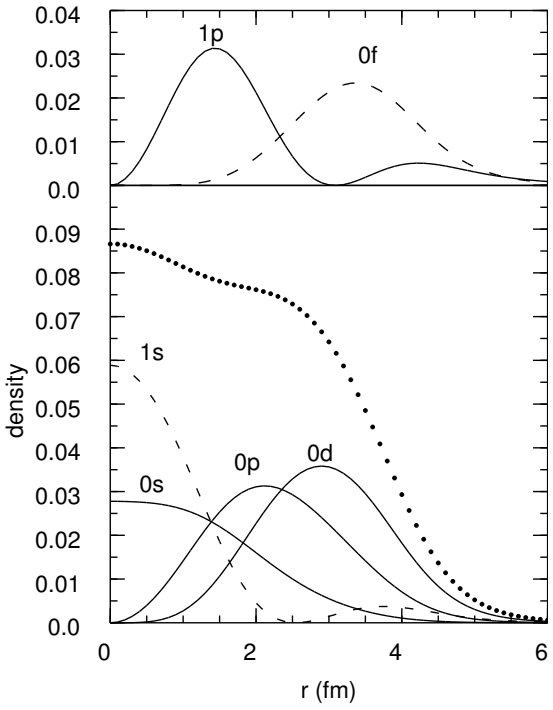

Figure 11: The point-proton density (points) of ^{40}Ca in the SKX model with a closed shell configuration. The total density is decomposed in terms of the contributions from the individual filled orbitals. In the upper panel the densities for protons in the orbitals just above the Fermi-surface of ^{40}Ca are shown, for eight protons in the $0f_{7/2}$ orbit and for four protons in the $1p_{3/2}$ orbit.

specific shell model orbitals which are filled, we show in Fig. (12.11) the point-proton density of ^{40}Ca (points) obtained with SKX with the assumption that the $0s, 0p, 1s$ and $0d$ orbits are filled. The individual contributions of the filled orbits to the proton density are shown. The $0s$ and $1s$ are the contributions from two protons in each of these orbits respectively. The $0p$ indicates the sum of the four protons in the $0p_{3/2}$ orbit and two protons in the $0p_{1/2}$ orbit. The $0d$ indicates the sum of the six protons in the $0d_{5/2}$ orbit and four protons in the $0d_{3/2}$ orbit. In the top panel the densities associated with the (unfilled) valence orbits above the Fermi-surface are shown; $0f$ for eight protons in the $0f_{7/2}$ orbit and $1p$ for four protons in the $1p_{3/2}$ orbit.

For comparison between experimental and theoretial charge densities I consider in Fig. (12.12) a set of data for nuclei that cover a wide mass range and which for which there is the good electron scattering data: ^{28}Si from Ref. [21], ^{32}S from Ref. [22] (circles) and Ref. [23] (squares), ^{40}Ca and ^{48}Ca from Ref. [24], ^{50}Ti and ^{52}Cr from Ref. [25], ^{54}Fe from Ref. [26], ^{58}Ni from Refs. [27] (circles) and [26] (squares),

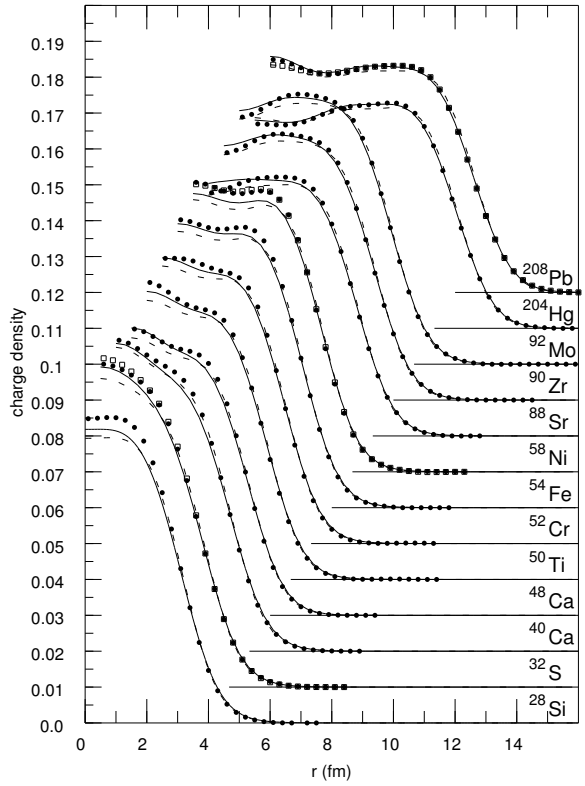

Figure 12: Experimental charge-density distributions (filled circles) compared with the SKX (dashed lines) and SKM* (solid lines) calculations. The charge density units are e fm^{-3}. Beyond ^{28}Si the curves and data have been progressively offset by 1 fm and 0.01 in the charge density. The data are discussed in the text.

^{88}Sr from Ref. [28], ^{90}Zr from Ref. [29], ^{92}Mo from Ref. [30], ^{204}Hg from Ref. [31], and ^{208}Pb from Refs. [32] (circles) and [33] (squares). The data are compared to the SKX (dashed lines) and SKM* (solid lines) are calculations. Both SKX and SKM* nicely reproduce the nucleus-dependent oscillations. The hamiltonian parameters are obtained from fits to the rms charge radii, binding energies and excited state energies of these nuclei. Thus the good agreement between experiment and theory for the nucleus-dependent oscillations observed in Fig. (12.12) are not a result of a "fit" to these data but arise naturally from the underlying shell structure.

The main difference between the SKX and SKM* results is that the interior density is about 5% higher with SKM* compared to SKX, with SKM* in best overall agreement with experiment. Close inspection of the curves in Fig. (12.12) in the region where the density falls off reveals a slightly larger surface diffuseness for SKM* com-

pared to SKX (the dashed line for SKX is slightly steeper than the line for SKM* in the surface). The correlation between the increased interior height with the increased diffuseness (when the rms radius is the same) is consistent with what is expected from the Fermi model shown in Fig. 3.2. The change between SKX and SKM* corresponds to a $\Delta a = 0.036$ fm for ^{208}Pb. The change in the diffuseness is connected to the difference in the density-dependent part of the hamiltonians, namely $[\rho(r)]^{1/2}$ for SKX and $[\rho(r)]^{1/6}$ for SKM*. There is agreement between experiment and theory to an accuracy of about 2% or better for $r > 1$ fm with SKM*. As discussed above, this is about the level of the accuracy with which these densities can be experimentally determined.

In the overview of Fig. (12.12) one can observe several interesting features associated with how the quantum waves change with shell structure and mass. Between ^{28}Si and ^{32}S in the sd shell there is a large increase in the interior density due to the filling of the $1s_{1/2}$ orbital (see also [23]). Likewise between ^{204}Hg and ^{208}Pb there is a large increase in the interior related to the filling of the $2s_{1/2}$ orbital. Between ^{40}Ca and ^{48}Ca one observes a redistribution of the charge (proton) density due to the interaction with the valence $0f_{7/2}$ neutrons. The theoretical density distributions for the sequence ^{48}Ca, ^{50}Ti, ^{52}Cr and ^{54}Fe show a smoothly varying trend due to dominance of the proton $0f_{7/2}$ subshell filling.

12.4.4 Displacement energies

The displacement energy is the binding energy difference between mirror nuclei (those with the same atomic number A but with the proton number Z and neutron number N interchanged). For a given mass A and isospin T the displacement energy is:

$$D(A,T) = BE(A,T_z^<) - BE(A,T_z^>), \tag{12.33}$$

where $T = \mid T_z^< \mid = \mid T_z^> \mid$, $BE(A,T_z^<)$ is the binding energy of the proton-rich nucleus and $BE(A,T_z^>)$ is the binding energy of the neutron-rich nucleus. If the nuclear force is charge symmetric, then this binding energy difference can be related to the well-understood Coulomb interaction between the protons. However, it was shown by Nolen and Schiffer [34] that there is a systematic increase in the experimental displacement energies compared to those calculated with a charge symmetric strong interaction (the Nolen-Schiffer anomaly). In the usual HF calculation one has both direct and exchange terms in the Coulomb-energy density functional. For the exchange one uses the Fermi-gas approximation which is a good approximation to the exact calculation [35]. The ground-state displacement energies obtained with the Coulomb plus Coulomb-exchange HF approach (from the SKXce interaction of [14]) are shown on the right-hand side of Fig. (12.13). One observes the systematic deviation between experiment and theory associated with the Nolen-Schiffer anomaly. For the heaviest

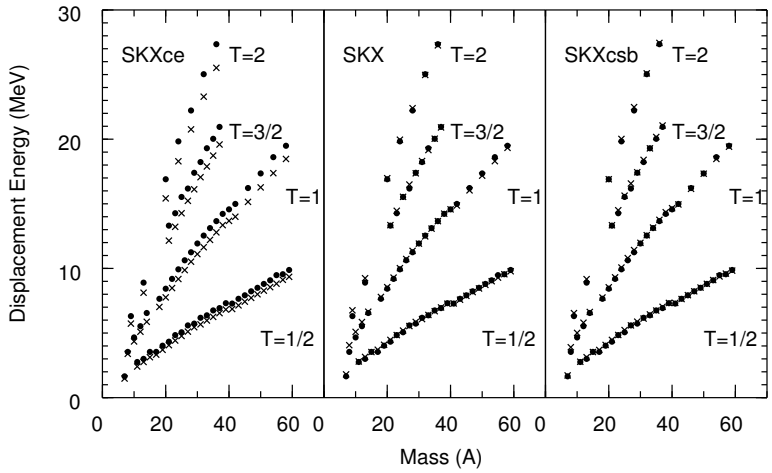

Figure 13: Ground-state displacement energies as a function of A for SKXce (with the normal Coulomb exchange term), SKX (without the exchange term) and SKXcsb (with the exchange term and with a CSB interaction). The experimental data are filled circles and the calculations are given as crosses.

nuclei the ratio shown in Fig. (12.14) goes to a constant value of about 1.06. It is well known [34] that the displacement energies are sensitive to the rms charge radii; the SKX interactions reproduce the experimental charge radii of ^{16}O, ^{40}Ca and ^{48}Ca to better than one percent (see Fig. 10 of [14]). The displacement energies are also sensitive to the rms radius of the valence orbits, and the SKX interactions give radii for the $d_{5/2}$ orbit in ^{17}O and the $0f_{7/2}$ orbit in ^{41}Ca which are within 2% of those deduced from the magnetic electron scattering form factors [36].

In the fit to closed-shell nuclei the displacement energy is represented by the pair of nuclei ^{48}Ni-^{48}Ca. The binding energy of ^{48}Ni is not measured but can be extrapolated to within an uncertainly of a few hundred keV from the $0f_{7/2}$ shell displacement energy systematics [37], [38], [39], [40], [41]. The recent discovery of ^{48}Ni [42] is consistent with the mass obtained from the $0f_{7/2}$ extrapolations.

In order to improve agreement with experiment it was found that the HF theory could be improved in two ways. One of them consists of leaving out the Coulomb exchange term, with the result shown in the middle panel of Figs. (12.13) and (12.14). This may be interpreted as a correction from nuclear correlation (configuration mixing) which happens to cancel the exchange term. This has been discussed in the general HF framework by Bulgac and Shaginyan [43], [44], [45] in terms of a surface-vibration contribution to the Coulomb correlation energy. I note that the relativistic approach leaves out the Coulomb exchange by default, and that most Woods-Saxon programs [46], [47] leave out the Coulomb exchange.

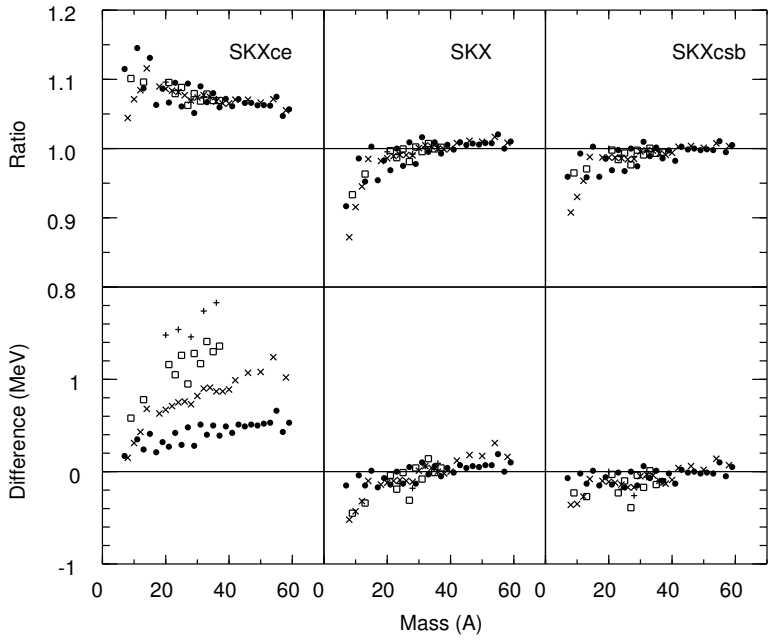

Figure 14: Top: the ratio experiment/theory for the data shown in Fig. (12.13); Bottom: the difference experiment–theory. The symbols are filled circles for $T = 1/2$, crosses for $T = 1$, squares for $T = 3/2$ and plus signs for $T = 2$.

Another way to improve agreement with experiment is to add a charge-symmetry breaking (CSB) term to the Skyrme interaction which can be expressed as a change to the proton-proton (pp) and neutron-neutron (nn) s-wave interactions:

$$V^{pp}_{\rm Skyrme} = t_0(1 - x_0)(1 + x_a)\delta$$

and

$$V^{nn}_{\rm Skyrme} = t_0(1 - x_0)(1 - x_a)\delta, \tag{12.34}$$

where x_a is a parameter to be determined.

The $A = 48$ closed shell nuclei require $x_a = -0.014 \pm 0.002$ for the interaction called SKXcsb The results for the all displacement energies are shown on the right-hand side of Figs. (12.13) and (12.14).

A correct description of the displacement energies within the mean field approximation is obviously important for understanding the position of the proton drip lines. $A = 99$ is the heaviest $T = 1/2$ isobaric doublet for which the proton-rich nucleus is expected to be bound. The calculated displacement energies for $A = 99$ are -13.54 MeV (SKXce), -14.03 MeV MeV (SKX) and -14.15 MeV (SKXcsb). The introduction of the extra terms in the Skyrme hamiltonian which are needed for the displacement energies, also has an influence on the neutron drip line; for example

the binding energy of ^{176}Sn is predicted to be -1158.0 MeV (SKXce), -1149.0 MeV (SKX) and -1148.4 MeV (SKXcsb).

The SKXcsb interaction should ultimately be related to the CSB nucleon-nucleon (NN) scattering data. Analysis of the NN scattering data together with a model for the NN interaction gives [48], [49] a value of $\Delta a_{CSB} = a_{pp} - a_{nn} = 1.5 \pm 0.5$ fm for the difference in the *pp* and *nn* scattering lengths. Modern NN potentials such as the AV18 [50] and CDbonn99 [51] are designed to reproduce this difference. It is not easy to interpret the CSB contribution to the displacement energies directly in terms of a NN potential due the short-range nuclear correlations and their dependence on the strong NN potential. Probably the most realistic way to do this is to consider the CSB contribution to the displacement energies obtained with the variational Monte Carlo approach for $A = 7$ [52] and the BHF approach for $A = 15$ and $A = 17$ [51]. For example, the CSB displacement energy for the $A = 17$, $d_{5/2}$ state is 92 keV with AV18 [51] to be compared with 355 keV with SKXcsb. From these comparisons one finds that the effect of the empirical CSB interaction obtained for SKXcsb is a factor of 3−4 larger than expected from AV18 or CDbonn99. Thus one concludes that either there is a significant NNN or many-body CSB contribution whose origin is unknown, or that a major part of the displacement energy anomaly is due to nuclear correlations. Possible many-body CSB effects at the quark level have recently been examined [53], [54].

The systematics associated with the Coulomb displacement energies can be used to obtain theoretical binding-energies of proton-rich nuclei from the experimental binding energies of neutron-rich nuclei. The displacement energies of Eq. (12.33) can be modeled on smooth systematics [38], [39], [55]; shell-model configuration mixing which contains the Coulomb and CSB interactions [37], [40], [41]; or on the mean-field models. One can combine the experimental binding energy for the neutron-rich nucleus $BE(A, T_z^>)_{exp}$ together with the calculated value for $D(A, T)$ to give an extrapolation for the proton-rich binding energy:

$$BE(A, T_z^<) = D(A, T)_{\text{theory}} + BE(A, T_z^>)_{exp}. \tag{12.35}$$

For most of the nuclei out to the proton drip line the binding energy $BE(A, T_z^>)_{exp}$ of the mirror neutron-rich nucleus is known to 100 keV or better. This method has been used to predict the binding energies and the drip line for $Z = 19 - 28$ [37], [41], [38] and $Z = 28 - 38$ [41], [56]. The latter calculations have been used [56] to study the rapid-proton (rp) capture path in the astrophysical explosive hydrogen burning process [57]. The rp-process in light nuclei depends upon theoretical calculations of the displacement energies of ground and excited states and upon the spectroscopic factors which enter into the (p,γ) reaction [58], [59].

References

[1] T. R. H. Skyrme. Philos. Mag. **1**, 1043 (1956); Nucl. Phys. **9**, 615 (1959); **9**, 635 (1959).

[2] D. Vautherin and D. M. Brink, Phys. Rev. C **5**, 626 (1972).

[3] C. B. Dover and N. Van Giai, Nucl. Phys. **A190**, 373 (1972).

[4] W. Kohn and L. J. Sham, Phys. Rev. **140** A1133 (1965).

[5] R. M. Dreizler and E. K. U. Gross, "Density Functional Theory: An Approach to the Quantum Many-Body Problem", (Springer, Berlin, 1990).

[6] M. M. Sharma, G. Lalazissis, J. Konig and P. Ring, Phys. Rev. Lett. **74**, 3744 (1995).

[7] B. Friedman and V. R. Pandharipande, Nucl. Phys. **A361**, 502 (1981).

[8] B. A. Brown, Phys. Rev. Lett. **85**, 5296 (2000).

[9] S. Typel and B. A. Brown, Phys. Rev. C **64**, 027302 (2001).

[10] B. A. Brown, W. A. Richter and R. Lindsay, Phys. Lett. B **483**, 49 (2000).

[11] S. Goriely, F. Tondeur and J. M. Pearson, At. Data Nucl. Data Sheets **77**, 311 (2001).

[12] J. D. Walecka, Ann. Phys. (N. Y.) **83**, 491 (1974).

[13] G. A. Lalazissis, J. König and P. Ring, Phys. Rev. C **55**, 540 (1997).

[14] B. A. Brown, Phys. Rev. C **58**, 220 (1998).

[15] S. O. Backman, G. E. Brown and J. A. Niskanen, Phys. Rep. **124**, 1 (1985).

[16] C. Mahaux, P. F. Bortignon, R. A. Broglia and C. G. Dasso, Phys. Rep. **120**, 1 (1985).

[17] I. Hamamoto, H. Sagawa and X . Z. Zhang, Phys. Rev. C **64**, 024313 (2001).

[18] J. Bartel, P. Quentin, M. Brack, C.Guet, and M. B. Hakansson, Nucl. Phys. **A386**, 79 (1982).

[19] H. de Vries, C. W. de Jager and C. de Vries, At. Data and Nucl. Data Tables **36**, 495 (1987).

[20] G. Fricke, C. Bernhardt, K. Heilig, L. A. Schaller, L. Shellenberg, E. B. Shera and C. W. de Jager, At. Data and Nucl. Data Sheets **60**, 177 (1995).

[21] H. Miessen, Ph.D. Thesis, University of Mainz, 1982 (unpublished).

[22] D. Rychel, Ph.D. Thesis, University of Mainz, 1983 (unpublished)

[23] J. Wesseling, C. W. de Jager, L. Lapikas, H. de Vries, L. W. Fagg, M. N. Harakeh, N. Kalantar-Nayestanaki, R. A. Lindgren, E. Moya De Guerra, and P. Sarriguren, Phys. Rev. **C55**, 2773 (1997)

[24] H. J. Emrich, Ph.D. Thesis, University of Mainz, 1983 (unpublished)

[25] J. W. Lightbody, Jr., J. B. Bellicard, J. M. Cavedon, B. Frois, D. Goutte, m. Huet, Ph. Leconte, A. Nakada, Phan Xuan Ho, S. K. Platchkov, S. Turck-Chieze, C. W. de Jager, J. J. Lapikas, and P. K. A. de Witt Huberts. Phys. Rev. **C27**, 113 (1983)

[26] H. D. Wohlfahrt, Habilitationsschrift, University of Mainz, 1976 (unpublished)

[27] G. Beuscher, Ph.D. Thesis, University of Mainz, 1983 (unpublished)

[28] G. Stephan, Ph.D. Thesis, University of Mainz, 1976 (unpublished)

[29] H. Rothhaas, Ph.D. Thesis, University of Mainz, 1976 (unpublished)

[30] B. Dreher, Phys. Rev. Lett **35**, 716 (1975)

[31] A. J. C. Burghardt, Ph.D. Thesis, University of Amsterdam, 1989 (unpublished)

[32] H. Euteneuer, J. Friedrich and N. Vögler, Nucl. Phys. **A298**, 452 (1978)

[33] J. L. Friar, J. Heisenberg and J. W. Negele, Proceedings of the June Workshop in Intermediate Energy Electromagnetic Interactions, edited by A. M. Bernstein, Massachusetts Institute of Technology (1977), p. 325

[34] J. A. Nolen and J.P. Schiffer, Ann. Rev. Nucl. Sci. **19**, 471 (1969).

[35] C. Titin-Schnaider and P. Quentin, Phys. Lett. **49B**, 397 (1974).

[36] T. Suzuki, H. Sagawa and A. Arima, Nucl. Phys. **A536**, 141 (1992)

[37] B. A. Brown, Phys. Rev. C **43**, R1513 (1991); C **44**, 924 (1991).

[38] B. J. Cole, Phys. Rev. C **54**, 1240 (1996).

[39] Phys. Rev. C **58**, 2831 (1998).

[40] W. E. Ormand, Phys. Rev. C **53**, 214 (1996); Phys. Rev. C **55**, 2407 (1997).